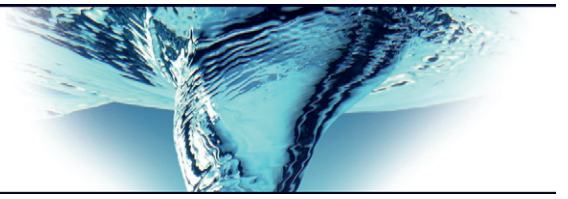
CrossMark

J. Fluid Mech. (2017), *vol.* 820, R1, doi:10.1017/jfm.2017.239



On the orientational dependence of drag experienced by spheroids

Sathish K. P. Sanjeevi[1] **and Johan T. Padding**[1,2,†]

[1]Process and Energy Department, Delft University of Technology, Leeghwaterstraat 39, 2628 CB Delft, The Netherlands

[2]Department of Chemical Engineering and Chemistry, Eindhoven University of Technology, 5600 MB Eindhoven, The Netherlands

(Received 3 February 2017; revised 7 April 2017; accepted 8 April 2017; first published online 2 May 2017)

The flow around different prolate (needle-like) and oblate (disc-like) spheroids is studied using a multi-relaxation-time lattice Boltzmann method. We compute the mean drag coefficient $C_{D,\phi}$ at different incident angles ϕ for a wide range of Reynolds numbers (Re). We show that the sine-squared drag law $C_{D,\phi} = C_{D,\phi=0^\circ} + (C_{D,\phi=90^\circ} - C_{D,\phi=0^\circ}) \sin^2 \phi$ holds up to large Reynolds numbers, $Re = 2000$. Further, we explore the physical origin behind the sine-squared law, and reveal that, surprisingly, this does not occur due to linearity of flow fields. Instead, it occurs due to an interesting pattern of pressure distribution contributing to the drag at higher Re for different incident angles. The present results demonstrate that it is possible to perform just two simulations at $\phi = 0^\circ$ and $\phi = 90^\circ$ for a given Re and obtain particle-shape-specific C_D at arbitrary incident angles. However, the model has limited applicability to flatter oblate spheroids, which do not exhibit the sine-squared interpolation, even for $Re = 100$, due to stronger wake-induced drag. Regarding lift coefficients, we find that the equivalent theoretical equation can provide a reasonable approximation, even at high Re, for prolate spheroids.

Key words: multiphase and particle-laden flows, particle/fluid flow

1. Introduction

Industrial applications and real-life cases often involve suspensions of non-spherical particles, of either regular or irregular shapes. Prolate (needle-like) spheroids can be used to describe milled biomass particles, fibrous suspensions and submarine hulls. On the other hand, oblate (disc-like) particles can be used as an approximation to represent red blood cells. El Khoury, Andersson & Pettersen (2010, 2012) performed direct numerical simulations (DNS) with the flow perpendicular to the symmetry axis of the spheroid and investigated the wakes behind a prolate spheroid of ratio

† Email address for correspondence: J.T.Padding@tudelft.nl

© Cambridge University Press 2017

https://doi.org/10.1017/jfm.2017.239 Published online by Cambridge University Press

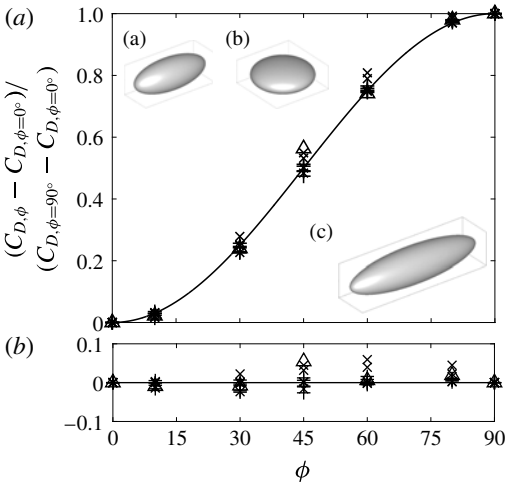


FIGURE 1. (*a*) The normalized drag coefficient $(C_{D,\phi} - C_{D,\phi=0^\circ})/(C_{D,\phi=90^\circ} - C_{D,\phi=0^\circ})$ plotted against the incident angle ϕ. The solid line indicates $\sin^2\phi$. Data include (a) a prolate spheroid (+) and (b) an oblate spheroid (×), both of aspect ratio 5/2, both for $Re = 0.1$, 10, 100, 1000 and 2000, and (c) a prolate spheroid of aspect ratio 4 (△) for $Re = 2000$. Averaged C_D values are used for cases with vortex shedding occurring at high Re. (*b*) The difference between the normalized drag coefficient and $\sin^2\phi$.

6 : 1. Hölzer & Sommerfeld (2009) and Zastawny *et al.* (2012) investigated different non-spherical particles at different flow incident angles at different Reynolds numbers (Re), albeit limited mainly to the steady flow regime. Very recently, Ouchene *et al.* (2016) proposed force correlations for prolate spheroids up to an aspect ratio of 32, again limited to steady flows with $Re \leqslant 240$. They reported an interesting finding that the drag coefficient C_D of the prolate spheroids follows a sine-squared interpolation between its extreme C_D values for $Re \leqslant 240$ for the reported aspect ratios. In this paper, we investigate this phenomenon more deeply and to higher Re.

Some authors define the Reynolds number Re_d based on the minimum thickness of the particle d_{min}. For this work, the Reynolds number is defined as $Re = |\boldsymbol{u}_\infty| d_{eq}/\nu$, where $\boldsymbol{u}_\infty$ is the uniform inlet velocity, ν is the kinematic viscosity of the fluid and d_{eq} is the diameter of the volume-equivalent sphere given by $d_{eq} = (6V_p/\pi)^{1/3}$, with V_p being the particle volume. The drag coefficient is defined as $C_D = |\boldsymbol{F}_D|/((1/2)\rho|\boldsymbol{u}_\infty|^2(\pi/4)d_{eq}^2)$. Here, $\boldsymbol{F}_D$ is the drag force acting on the particle and ρ is the fluid density. For any particle in the Stokes regime (Happel & Brenner 1983), based on linearity of the Stokes equations, the drag coefficient at different incident angles ϕ interpolates as

$$C_{D,\phi} = C_{D,\phi=0^\circ} + (C_{D,\phi=90^\circ} - C_{D,\phi=0^\circ}) \sin^2\phi. \tag{1.1}$$

Here, the subscript ϕ implies the value at that particular incident angle ϕ.

To motivate the reader, the drag on different spheroids is tested up to $Re = 2000$ and the mean values of C_D are plotted in figure 1. Surprisingly, the investigated particles follow sine-squared interpolation very well for both steady and unsteady regimes, even for Re as high as 2000. This interesting phenomenon appears to be similar to the Stokes regime prediction (1.1), as mentioned by Ouchene *et al.* (2016). We investigated the phenomenon in detail and found a plausible reason and also the

https://doi.org/10.1017/jfm.2017.239 Published online by Cambridge University Press

limitations of the sine-squared behaviour. Our findings at high Re, in combination with observations of Ouchene *et al.* (2016) for prolate spheroids up to aspect ratio 32, extend the validity of the drag law to both high-aspect-ratio prolate spheroids and high Re. This implies that, in many situations, the mean drag coefficient at any incident angle $C_{D,\phi}$ for a given Re can be obtained by just knowing two values, $C_{D,\phi=0^\circ}$ and $C_{D,\phi=90^\circ}$.

2. Numerical method

2.1. *Lattice Boltzmann method*

The fluid flow is simulated using a D3Q19 multi-relaxation-time (MRT) lattice Boltzmann method (LBM) (d'Humières *et al.* 2002). The MRT-LBM scheme solves the evolution of the particle distribution function $|f\rangle$,

$$|f(\boldsymbol{r}+\boldsymbol{e}_\alpha\Delta t, t+\Delta t)\rangle = |f(\boldsymbol{r}, t)\rangle - \boldsymbol{M}^{-1}\hat{\boldsymbol{S}}(|m(\boldsymbol{r}, t)\rangle - |m^{(eq)}(\boldsymbol{r}, t)\rangle), \tag{2.1}$$

for position $\boldsymbol{r}$ with discrete velocities $\boldsymbol{e}_\alpha$ in directions $\alpha = 1, 2, \ldots, 19$. Here, $\boldsymbol{M}$ is a 19×19 transformation matrix used to transform $|f\rangle$ from velocity space to moment space $|m\rangle$, with $|m\rangle = \boldsymbol{M}\cdot|f\rangle$; the ket vector $|\cdot\rangle$ implies a column vector. The relaxation matrix $\hat{\boldsymbol{S}} = \boldsymbol{M}\cdot\boldsymbol{S}\cdot\boldsymbol{M}^{-1}$ is a 19×19 diagonal matrix. The relaxation matrix $\hat{\boldsymbol{S}}$ utilizes different optimally chosen relaxation rates for different moments, thereby providing better stability compared with the single-relaxation-time LBM scheme (d'Humières *et al.* 2002). The matrices $\boldsymbol{M}$ and $\hat{\boldsymbol{S}}$ are similar to those of Huang *et al.* (2012). The kinematic viscosity of the fluid is set by the relaxation time τ as $\nu = c_s^2(\tau - 1/2)\Delta t$ and the pressure p is related to the density by $p = \rho c_s^2$. Uniform velocity in the z direction is prescribed at the inlet boundary based on the work of Hecht & Harting (2010). The sidewalls are prescribed with free-slip boundaries rather than periodic boundary conditions, which could cause the flow to deflect either up or down based on the inclination of the non-spherical particle (Hölzer & Sommerfeld 2009). The downstream (outlet) is specified with an axial-stress-free boundary condition with $\partial u_z/\partial z = 0$ (Aidun, Lu & Ding 1998). We use the linearly interpolated bounce-back scheme (Bouzidi, Firdaouss & Lallemand 2001; Lallemand & Luo 2003) to accurately consider the curved geometry of the particle. The improvement in solution accuracy is negligible between linear and quadratic interpolation schemes, provided that sufficient resolution is used (Pan, Luo & Miller 2006; Kruggel-Emden *et al.* 2016).

2.2. *Influence of grid resolution*

The influence of the grid resolution is tested with the flow around an isolated sphere. The normalized C_D is plotted in figure 2. Three different regimes are tested: (i) Stokes flow, (ii) intermediate Reynolds number, $Re = 100$, with a steady wake and (iii) high Reynolds number, $Re = 1000$, exhibiting a complex unsteady wake, and therefore the mean drag coefficient is shown. The influence of the resolution is stronger with increasing Re, as seen in figure 2. For $Re = 1000$, the observed C_D at resolution $d_{eq} = 40$ is 0.456 and is in good agreement with literature results: $C_D = 0.464$ from Vakarelski *et al.* (2016) and $C_D = 0.48$ from Ploumhans *et al.* (2002). This resolution information is considered in maintaining the minimum thickness d_{min} of our non-spherical particles at different Re. Due to the non-sphericity, the other dimension is always larger than the minimum thickness and therefore a good particle resolution is ensured.

https://doi.org/10.1017/jfm.2017.239 Published online by Cambridge University Press

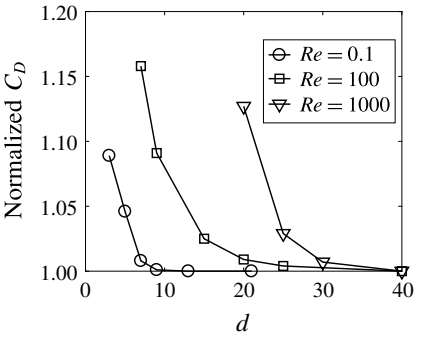


FIGURE 2. For a sphere, the normalized C_D as a function of the diameter d in lattice cells for different Re, showing convergence of the method. The normalization is made with respect to the highest resolution C_D.

3. Test of linearity for pressure and velocity fields

The drag law for Stokes flow (1.1) for non-spherical particles is based on the linearity of the Stokes equations in the creeping flow limit. As figure 1 shows, we observe that the mean C_D follows the same sine-squared behaviour even in regimes with a complex unsteady wake at Re as high as 2000. It has to be noted that all of the investigated geometries are axisymmetric, smooth and rounded. Although nonlinear effects dominate at higher Re, we first investigate whether the inherent smooth nature of the geometries results in cancellation of nonlinearity effects in the region close to the particle surface. In other words, we test whether the velocity and pressure fields for an arbitrary particle at incident angle ϕ obey the following conditions sufficiently close to the surface:

$$\boldsymbol{u}_\phi = \boldsymbol{u}_{\phi=0^\circ} \cos\phi + \boldsymbol{u}_{\phi=90^\circ} \sin\phi, \tag{3.1}$$

$$p_\phi - p_\infty = (p_{\phi=0^\circ} - p_\infty)\cos\phi + (p_{\phi=90^\circ} - p_\infty)\sin\phi. \tag{3.2}$$

Here, $\boldsymbol{u}_\phi$ is the velocity field and p_ϕ is the pressure field around the particle, based on the incoming flow $\boldsymbol{u}_\infty$ oriented at angle ϕ, as shown in figure 3. If (3.1) and (3.2) are true, the corresponding drag components, i.e. the viscous drag $C_{D\nu,\phi}$ and the pressure drag $C_{Dp,\phi}$, also follow the sine-squared law.

Throughout this paper, from the three-dimensional simulations, the flow fields are analysed along the meridional plane. The meridional plane contains the axis of symmetry of the particle at different incident angles and the inflow velocity vector $\boldsymbol{u}_\infty$. Of the different particles tested, we consider the prolate spheroid of aspect ratio 5/2 for the linearity study. A special case of $\phi = 30^\circ$ is tested along the meridional plane. The velocity and pressure fields from the theoretical linear combination in (3.1) and (3.2) are compared with the actual flow field from the simulations. Two cases, one for the Stokes flow at $Re = 0.1$ and another exhibiting steady flow, yet sufficiently large Re compared with the Stokes regime, $Re = 100$, are considered. The velocity fields based on the theory and the actual flow are given in figure 4. For Stokes flow, the linear superposition of velocity fields results in attached flow around the particle. There is a good match between the theoretical and actual fields, with deviations of up to 2 %. At $Re = 100$, the flow field exhibits attached flow for $\phi = 0^\circ$ due to streamlining and a strong recirculation for $\phi = 90^\circ$. In figure 4(*d*), their linear

https://doi.org/10.1017/jfm.2017.239 Published online by Cambridge University Press

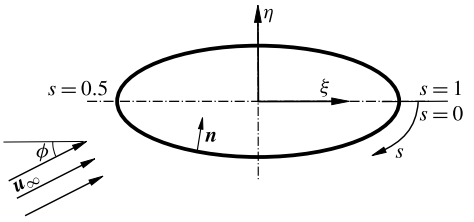


FIGURE 3. The local coordinate system (ξ, η) of the ellipsoidal section. Here, s is the normalized distance along the circumference and $\boldsymbol{n}$ is the inward facing local unit normal vector. The simulations are performed in a rectangular domain with the particle rotated for different incident angles. For clarity and consistency, the results are analysed in the local coordinate system of the section (ξ, η).

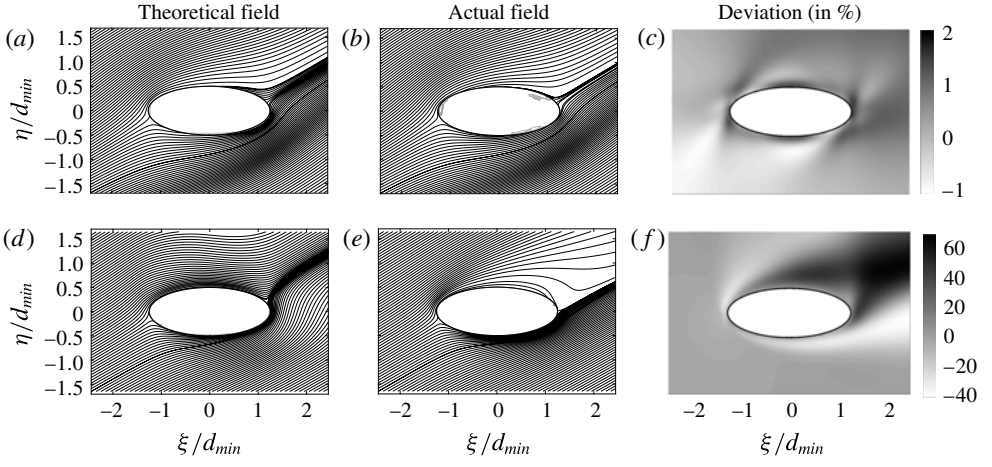


FIGURE 4. The theoretical ($\boldsymbol{u}_{th}$) and actual ($\boldsymbol{u}_{act}$) velocity fields and the deviation between these fields for $Re = 0.1$ (*a–c*) and $Re = 100$ (*d–f*). The deviation is computed as $\|\boldsymbol{u}_{th} - \boldsymbol{u}_{act}\|/\|\boldsymbol{u}_\infty\|$ in %. It should be noted that the deviation scales are different for different Re.

combination for $\phi = 30°$ still appears to be attached, whereas the actual flow field as shown in figure 4(*e*) exhibits recirculation in the wake of the particle. There is a strong mismatch between the fields, as shown in figure 4(*f*), with deviations of up to 60 %.

At the same time, it is interesting to note that the viscous drag force resulting from the velocity field becomes increasingly independent of the incident angle ϕ at higher Re. Figure 5 shows the viscous and pressure drag components at $Re = 0.1$, 10 and 100 for the prolate spheroid of aspect ratio 5/2. Indeed, it is observed that the viscous effects become weakly dependent on the incident angle ϕ at $Re = 10$. Eventually, at $Re = 100$, the viscous drag becomes independent of ϕ compared with change in the pressure drag, with $C_{Dv,\phi} \approx C_{Dv,\phi=0°} \approx C_{Dv,\phi=90°}$. This implies that the dependence of the drag on the incident angle of the particle, ϕ, at higher Re, is purely coupled to the ϕ dependence of the pressure drag. Therefore, we next focus on the pressure coefficient on the surface of the meridional plane section.

The pressure coefficient is defined as $C_p = (p - p_\infty)/(1/2\rho|\boldsymbol{u}_\infty|^2)$, with pressure p measured on the surface and p_∞ the pressure at the far field. The pressure coefficient

https://doi.org/10.1017/jfm.2017.239 Published online by Cambridge University Press

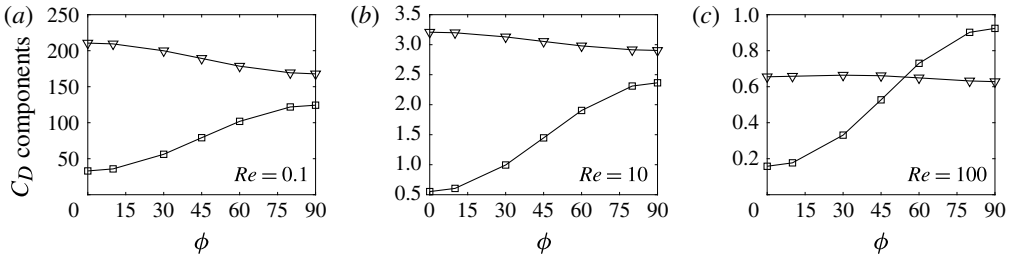


FIGURE 5. Viscous (▽) and pressure (□) components of the drag coefficient as a function of the incident angle ϕ at (*a*) $Re = 0.1$, (*b*) $Re = 10$ and (*c*) $Re = 100$.

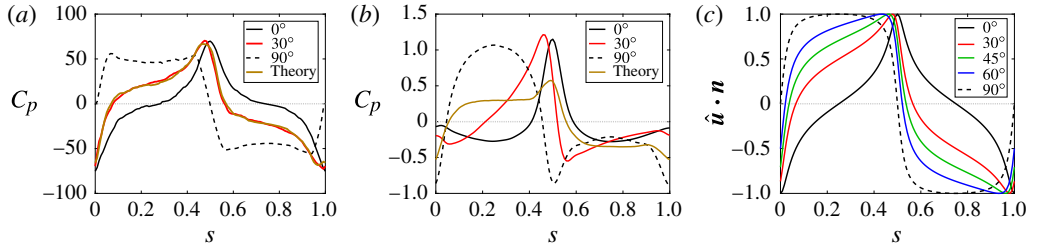


FIGURE 6. Distribution of C_p against normalized distance s along the circumference of the meridional section for (*a*) $Re = 0.1$ and (*b*) $Re = 100$. (*c*) Surface normal projections $\hat{\boldsymbol{u}} \cdot \boldsymbol{n}$ for different incident angles ϕ. It should be noted that the linearity theory matches perfectly with simulations for $Re = 0.1$ and shows strong mismatch for $Re = 100$. For the different values of ϕ shown, one can note the matching trends of C_p at $Re = 0.1$ with $\hat{\boldsymbol{u}} \cdot \boldsymbol{n}$.

C_p is plotted as a function of the distance s along the circumference of the meridional section, normalized with the section circumference, as shown in figure 3. The C_p distributions on the section along the meridional plane of the spheroid are plotted for $Re = 0.1$ and $Re = 100$ in figures 6(*a*) and 6(*b*) respectively. Referring to figure 3, the $\boldsymbol{u}_\infty$ at $\phi = 0°$ is along the $+\xi$ axis, and the C_p peaks are observed near $s = 0.5$ in figure 6(*a*,*b*), which is at the leading edge of the spheroid for that incident angle. At $Re = 0.1$, we observe an exact match between C_p using the linearity theory (3.2) and the actual simulation for $\phi = 30°$. At $Re = 100$, the actual C_p distribution for $\phi = 30°$ is different compared with the distribution based on linearity theory, as seen in figure 6(*b*). Therefore, it can be concluded that it is not due to linearity that the drag law shows sine-squared behaviour at higher Re.

4. Reason for the sine-squared drag law at higher *Re*

Again, we consider the meridional section of the prolate spheroid of aspect ratio 5/2 for this study. We hypothesize that the C_p distribution takes the form

$$C_p = -m + (1 + m)(\hat{\boldsymbol{u}} \cdot \boldsymbol{n})^k. \tag{4.1}$$

Here, m and k are constants, $\hat{\boldsymbol{u}} = \boldsymbol{u}_\infty / |\boldsymbol{u}_\infty|$ is the orientation of the far-field flow direction and $\boldsymbol{n}$ is the inward facing local unit normal vector, as in figure 3. The above form $-m + (1 + m)(\hat{\boldsymbol{u}} \cdot \boldsymbol{n})^k$ is inspired by the inviscid flow around a sphere,

https://doi.org/10.1017/jfm.2017.239 Published online by Cambridge University Press

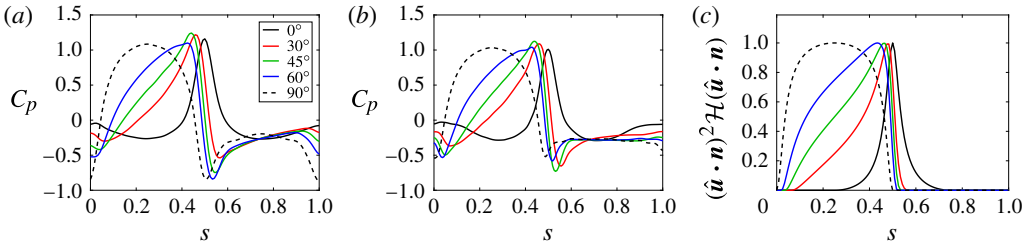


FIGURE 7. Distributions of C_p at (*a*) $Re = 100$ and (*b*) $Re = 2000$ (time averaged), and (*c*) second-power surface normal projections $(\hat{\boldsymbol{u}}\cdot\boldsymbol{n})^2\mathcal{H}(\hat{\boldsymbol{u}}\cdot\boldsymbol{n})$ versus the normalized distance s along the circumference of the meridional section for different values of ϕ.

where $C_p = 1 - c\sin^2\theta$, with $c = 9/4$ and the θ measured from the stagnation point. For a sphere, $\hat{\boldsymbol{u}}\cdot\boldsymbol{n} = \cos\theta$, and rearranging terms with $m = c - 1$, the C_p distribution for a sphere becomes $C_p = -m + (1+m)(\hat{\boldsymbol{u}}\cdot\boldsymbol{n})^2$. A more general form is considered in our case with an arbitrary exponent k.

The term $-m$ acts as a negative offset and the term $(1 + m)$ acts as a scaling factor, such that $C_p = 1$ at the stagnation point ($\hat{\boldsymbol{u}}\cdot\boldsymbol{n} = 1$), as would be expected from Bernoulli's law at the point where $\boldsymbol{u} = \boldsymbol{0}$. For increasing Re, the high-pressure region localizes more around the stagnation point, and this can be confirmed by comparing the C_p distribution for $\phi = 0°$ at $Re = 0.1$ and 100 in figures 6(*a*) and 6(*b*) respectively. Moreover, for $Re \gg 1$, figure 7(*a*,*b*) shows that the dominant part of the pressure drag originates from the front side of the particle ($\hat{\boldsymbol{u}}\cdot\boldsymbol{n} > 0$, see figure 6*c*), and therefore we focus on this region. For $Re \gg 1$, we choose $k = 2$. The value $k = 2$ is inspired by inviscid irrotational flow theory, as discussed above, although the flow is not exactly inviscid. The distributions of C_p for $Re = 100$, $Re = 2000$ (time averaged) and $(\hat{\boldsymbol{u}}\cdot\boldsymbol{n})^2\mathcal{H}(\hat{\boldsymbol{u}}\cdot\boldsymbol{n})$ are given in figures 7(*a*), 7(*b*) and 7(*c*) respectively. Here, $\mathcal{H}$ is the Heaviside step function, given by

$$\mathcal{H}(x) = \begin{cases} 1 & \text{if } x > 0, \\ 0 & \text{otherwise.} \end{cases} \tag{4.2}$$

The term $\mathcal{H}(\hat{\boldsymbol{u}}\cdot\boldsymbol{n})$ is introduced above to consider only the front side of the particle projected to the inflow.

It can be observed that the maximum values of C_p for different values of ϕ are nearly the same and close to 1, as expected at the stagnation point in inviscid flow. Moreover, the overall trends of the C_p curves in figure 7(*a*,*b*) and the $(\hat{\boldsymbol{u}}\cdot\boldsymbol{n})^2\mathcal{H}(\hat{\boldsymbol{u}}\cdot\boldsymbol{n})$ in figure 7(*c*) are almost similar, including the trends of curvature. Actually, for the pressure drag, we specifically need to look at the surface projection of C_p along the flow direction, i.e. $C_{p,drag} = C_p\hat{\boldsymbol{u}}\cdot\boldsymbol{n}$. The similarity between $C_{p,drag}$ and $(\hat{\boldsymbol{u}}\cdot\boldsymbol{n})^3$ for different angles can be observed in figure 8(*a–c*). The trends agree well for different incident angles. Further, the C_p and $C_{p,drag}$ distributions for $Re = 100$ and $Re = 2000$ indicate that they are self-similar and independent of Re, at least for the front side of the particle ($\hat{\boldsymbol{u}}\cdot\boldsymbol{n} > 0$). It should be noted that the influence of the offset m is less significant for $C_{p,drag}$ than it is for C_p. Moreover, the precise value of m may be position- and incident-angle-dependent, but its variation is negligible compared with the overall variation in the pressure drag. This is shown explicitly in figure 9, where the measured C_p distributions are compared with our proposed C_p form computed as

https://doi.org/10.1017/jfm.2017.239 Published online by Cambridge University Press

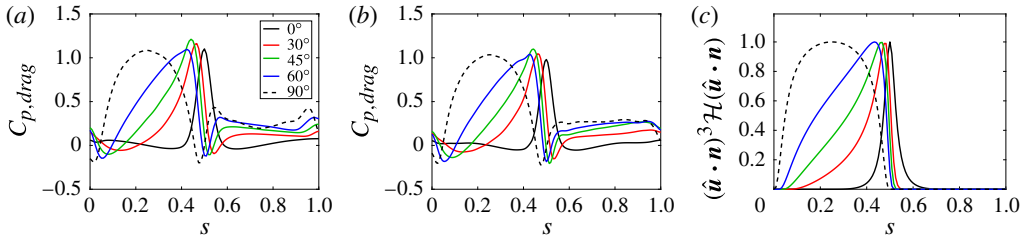


FIGURE 8. Distributions of $C_{p,drag}$ at (*a*) $Re = 100$ and (*b*) $Re = 2000$ (time averaged), and (*c*) third-power surface normal projections $(\hat{\boldsymbol{u}}\cdot\boldsymbol{n})^3\mathcal{H}(\hat{\boldsymbol{u}}\cdot\boldsymbol{n})$ versus the normalized distance s along the circumference of the meridional section for different values of ϕ.

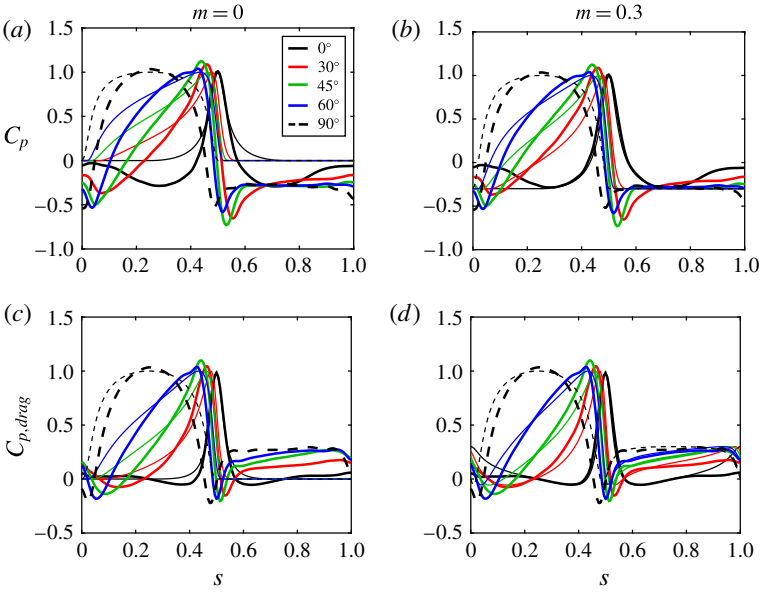


FIGURE 9. Quantitative comparison of the C_p (*a*,*b*) and $C_{p,drag} = C_p\hat{\boldsymbol{u}}\cdot\boldsymbol{n}$ (*c*,*d*) from the proposed theory ((4.1), thin lines) with the actual measurements at $Re = 2000$ (thick lines). We used $m = 0$ (*a*,*c*) and $m = 0.3$ (*b*,*d*). It should be noted that the influence of the value of m is weaker for $C_{p,drag}$ compared with C_p.

$C_p = -m + (1+m)(\hat{\boldsymbol{u}}\cdot\boldsymbol{n})^2\mathcal{H}(\hat{\boldsymbol{u}}\cdot\boldsymbol{n})$ and the $C_{p,drag}$ accordingly. It can be observed that the value of m influences C_p considerably. However, its influence on $C_{p,drag}$ is much weaker, and, therefore, we proceed with $m = 0$ in upcoming steps.

The term $C_{p,drag}$ corresponds to the local contribution of pressure to the sectional pressure drag. Therefore, we require integrals to compute the total pressure drag due to this section. We define the integral of kth power of projection $\hat{\boldsymbol{u}}\cdot\boldsymbol{n}$ for the front side of the section as

$$b_k = \int_0^1 (\hat{\boldsymbol{u}}\cdot\boldsymbol{n})^k\mathcal{H}(\hat{\boldsymbol{u}}\cdot\boldsymbol{n})\,\mathrm{d}s. \tag{4.3}$$

An interesting property is that the integral of the second power of projection, b_2, exactly obeys sine-squared behaviour for different values of ϕ. This can be written

https://doi.org/10.1017/jfm.2017.239 Published online by Cambridge University Press

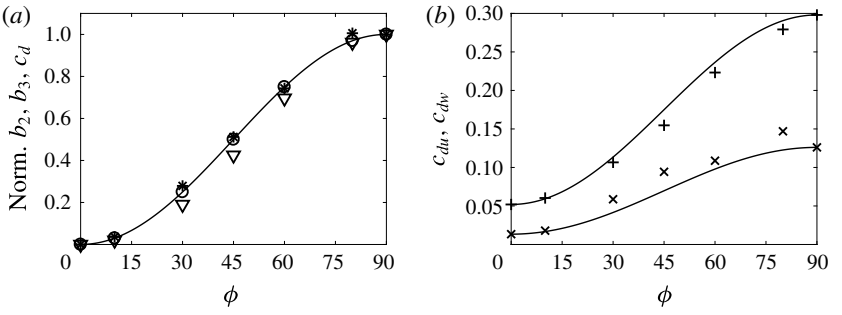


FIGURE 10. For a prolate spheroid of aspect ratio 5/2: (*a*) the normalized $b_{2,\phi}$ (○), $b_{3,\phi}$ (▽), sectional pressure drag $c_{d,\phi}$ at $Re = 2000$ (∗) and $\sin^2\phi$ (solid line); (*b*) components of sectional pressure drag $c_{d,\phi}$ at $Re = 2000$ decomposed into upstream drag $c_{du,\phi}$ (+) and wake side drag $c_{dw,\phi}$ (×), together with their corresponding sine-squared interpolating curves. It should be noted that the trends of $b_{3,\phi}$ and $c_{du,\phi}$ are similar, both under their respective sine-squared curves.

as $b_{2,\phi} = b_{2,\phi=0^\circ} + (b_{2,\phi=90^\circ} - b_{2,\phi=0^\circ})\sin^2\phi$ and is shown in figure 10(*a*). This law holds for the family of ellipsoidal sections and is independent of aspect ratio. This can also be confirmed from the fact that the C_p distribution is proportional to $\hat{\boldsymbol{u}}\cdot\boldsymbol{n}$ in Stokes flow (see figure 6*a*,*c*) and therefore $C_{p,drag} = C_p\hat{\boldsymbol{u}}\cdot\boldsymbol{n}$ is proportional to $(\hat{\boldsymbol{u}}\cdot\boldsymbol{n})^2$.

As per our earlier observation, at higher Re, the $C_{p,drag}$ distribution is proportional to $(\hat{\boldsymbol{u}}\cdot\boldsymbol{n})^3$. However, the integral $b_{3,\phi}$ does not exactly hold sine-squared behaviour, as shown in figure 10(*a*). It trends slightly below the sine-squared curve. The equivalent of $b_{3,\phi}$ is the sectional pressure drag from the upstream side of the section, which we compare in the upcoming steps. We define sectional pressure drag integrated over the circumference of an ellipsoidal section as

$$c_d = \int_0^1 C_{p,drag}\,\mathrm{d}s. \tag{4.4}$$

We then decompose c_d into upstream side (c_{du}) and wake side (c_{dw}) as

$$c_{du} = \int_0^1 C_{p,drag}\mathcal{H}(\hat{\boldsymbol{u}}\cdot\boldsymbol{n})\,\mathrm{d}s \quad \text{and} \quad c_{dw} = \int_0^1 C_{p,drag}\mathcal{H}(-\hat{\boldsymbol{u}}\cdot\boldsymbol{n})\,\mathrm{d}s. \tag{4.5a,b}$$

The above integrals for different incident angles ϕ, i.e. $c_{du,\phi}$ and $c_{dw,\phi}$, for $Re = 2000$ are plotted in figure 10(*b*) together with their corresponding sine-squared interpolation curves based on the end values. As seen from figure 10(*a*,*b*), the upstream drag $c_{du,\phi}$ trend is very similar to $b_{3,\phi}$ and both are slightly below their respective sine-squared curves. At the same time, the wake-induced drag component $c_{dw,\phi}$ values are slightly above their respective sine-squared curves at the intermediate angles, i.e. $0^\circ < \phi < 90^\circ$. Therefore, the wake drag adequately compensates the upstream drag proportionately at the intermediate angles, thereby making the total section drag appear to scale in a sine-squared manner. The normalized sectional pressure drag $c_{d,\phi}$ for different angles for $Re = 2000$ itself follows a near sine-squared pattern, as shown in figure 10(*a*). The spheroid by itself is made of different such ellipsoidal sections, each obeying sine-squared behaviour of different scales and altogether giving the total drag sine-squared behaviour. We have tested the reasoning in this section for different aspect ratio prolate spheroids, and found similar dependences of $C_{p,drag}$ with $(\hat{\boldsymbol{u}}\cdot\boldsymbol{n})^3\mathcal{H}(\hat{\boldsymbol{u}}\cdot\boldsymbol{n})$ for different values of ϕ.

https://doi.org/10.1017/jfm.2017.239 Published online by Cambridge University Press

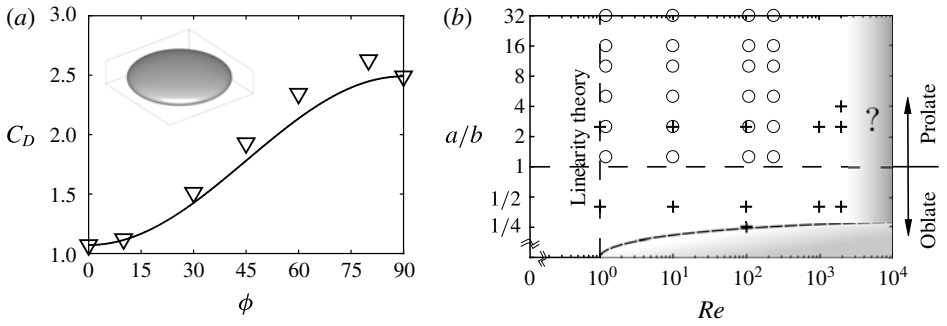


FIGURE 11. (*a*) Plot of C_D against ϕ at $Re = 100$ for an oblate spheroid of aspect ratio 4 ($\triangledown$) and the corresponding sine-squared interpolating curve (solid line); (*b*) the tested data points (+) and the *plausible* valid region for sine-squared scaling (unshaded). The valid region is based on our results and the data of Ouchene *et al.* (2016) for prolate spheroids up to aspect ratios of 32 and $Re = 240$ ($\bigcirc$). The ratio a/b is the ratio of lengths parallel and orthogonal to the axis of rotation.

4.1. *Limitations and comments*

In the introduction, we showed results for prolate spheroids of different aspect ratios and an oblate spheroid of aspect ratio 5/2. However, increasing the aspect ratio for an oblate spheroid results in an increasing digression from the sine-squared drag law, even at moderate Re. The C_D results for an oblate spheroid of aspect ratio 4 at $Re = 100$ are presented in figure 11(*a*). Clearly, a non-monotonic dependence of C_D on the incidence angle ϕ is observed. The observed maximum deviation is around 10 % at $\phi = 60^\circ$ against the sine-squared curve. The reason why the drag law fails for flatter discs can be explained by our earlier observation that the wake has a higher drag contribution at intermediate angles $0^\circ < \phi < 90^\circ$ (see c_{dw} in figure 10*b*) when compared with the sine-squared curve. The flat-disc-like geometry experiences a stronger wake, amplifying the effect strongly. If we assume a 10 % deviation to be the limit of applicability, the oblate spheroid of aspect ratio 4 is at the bounding limit for the drag law. On the other hand, prolate spheroids of larger aspect ratio, as shown in the introduction, still obey the sine-squared behaviour even at $Re = 2000$, due to the weaker wake side drag. A sketch of the plausible valid region of the sine-squared behaviour is shown in figure 11(*b*). We have also tested a capsule-like spherocylinder of aspect ratio 4 and it also exhibits sine-squared drag scaling at high Re, due to a closer resemblance to a prolate spheroid. The C_D results from this work will be published as correlations dependent on Re and ϕ in a separate paper. Since the prolate spheroid of aspect ratio 4 is simulated only for $Re = 2000$, the corresponding results are given here, with $C_{D,\phi=0^\circ} = 0.147$ and $C_{D,\phi=90^\circ} = 1.105$.

The $Re = 2000$ limit for the tested particles is rather limited by the LBM solver and not by the flow physics itself. We believe that the drag law might hold to even higher Re. However, flow fields are indeed complex for high Re and the extent to which the drag law is valid needs further investigation. For example, Jiang *et al.* (2015) simulated flow around a 6 : 1 prolate spheroid at $\phi = 45^\circ$ at $Re = 3000$ based on the minor diameter. They reported a side force, almost 75 % of the magnitude of the drag force, perpendicular to the meridional plane. This indicates that the flow is highly asymmetric about the meridional plane. However, they did not investigate the incident angle dependence of the drag force. To what extent their reported flow asymmetries

https://doi.org/10.1017/jfm.2017.239 Published online by Cambridge University Press

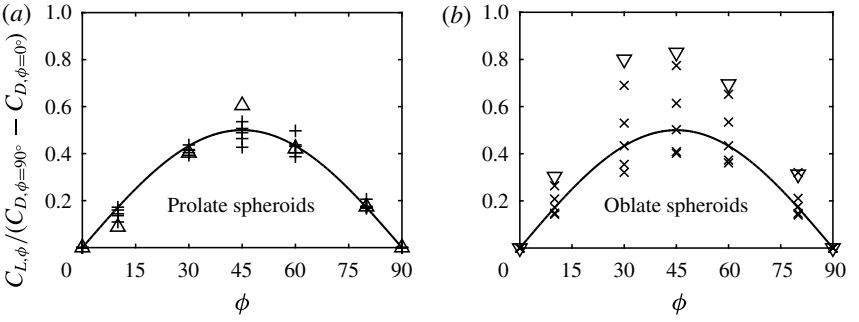


FIGURE 12. The normalized lift coefficient $C_{L,\phi}/(C_{D,\phi=90^\circ} - C_{D,\phi=0^\circ})$ plotted against the incident angle ϕ. The solid line indicates $\sin\phi\cos\phi$. (*a*) Prolate spheroid of aspect ratio 5/2 for $Re = 0.1$, 10, 100, 1000 and 2000 (+); prolate spheroid of aspect ratio 4 at $Re = 2000$ ($\triangle$); (*b*) oblate spheroid of aspect ratio 5/2 for $Re = 0.1$, 10, 100, 1000 and 2000 ($\times$); oblate spheroid of aspect ratio 4 at $Re = 100$ ($\triangledown$). It should be noted that the oblate spheroids are experiencing stronger deviations compared with prolate spheroids.

might influence the sine-squared drag behaviour is not yet known and therefore needs further investigation.

5. Lift forces

Besides drag, any non-spherical particle at an inclination with respect to a uniform flow will experience lift. Here, we provide a concise section with interesting observations and comments regarding the lift forces.

We define the lift coefficient as $C_L = |\boldsymbol{F}_L|/((1/2)\rho|\boldsymbol{u}_\infty|^2(\pi/4)d_{eq}^2)$, with F_L being the measured lift force. For a particle in the Stokes regime, based on linearity theory, the C_L at an incident angle ϕ is

$$C_{L,\phi} = (C_{D,\phi=90^\circ} - C_{D,\phi=0^\circ})\sin\phi\cos\phi. \tag{5.1}$$

From our experience of the different non-spherical particles tested, equation (5.1) is still a reasonable approximation in the complete absence of C_L data for prolate spheroids, even at high Re, as seen in figure 12(*a*). The average of the absolute deviations between $C_{L,\phi}$ from the simulations and (5.1) is less than 15 % for the tested prolate spheroids at different Re. For oblate spheroids, with increasing aspect ratios, the deviations increase more, as seen in figure 12(*b*). For the oblate spheroid of aspect ratio 4 at $Re = 100$, the simulated C_L is much larger, by around 60 %, than the theory for the reasons already observed in figure 10(*b*). Similarly to the drag, the wake-induced force is also contributing strongly to the lift and thereby making the observed C_L much larger than the theory at intermediate incident angles.

There are different reasons why the incident angle dependence of the lift coefficient C_L cannot be exactly quantified in a predictable fashion like that of C_D. The order of magnitude of the lift coefficient depends on the difference of C_D at two extreme incident angles, i.e. $(C_{D,\phi=90^\circ} - C_{D,\phi=0^\circ})$, and goes to zero at the extreme ends of incident angles, i.e. at $\phi = 0^\circ$, 90°. However, for C_D at different incident angles ϕ, apart from the C_D difference term, there is an additional term giving a constant offset, i.e. C_D at $\phi = 0^\circ$. This implies that the variation of $C_{L,\phi}$ is much more sensitive than that of $C_{D,\phi}$. Therefore, any variation in pressure distribution at higher Re would be more amplified for C_L than for C_D. The C_L results from this work will be published as correlations dependent on Re and ϕ in a separate paper.

https://doi.org/10.1017/jfm.2017.239 Published online by Cambridge University Press

6. Conclusion

The flow around prolate and oblate spheroids of different aspect ratios was studied. We explored the sine-squared drag law in detail with a prolate spheroid of aspect ratio 5/2. We found that the reason for the drag law at high Re is not due to linearity theory, which results in an identical drag law in the Stokes regime. At high Re, the viscous drag becomes almost independent of the incident angle ϕ and the pressure drag is the only factor influenced by the incident angle ϕ. At high Re, the pressure distribution contributing to the drag shows a dependence on the surface normal orientation with the incoming flow in a consistent pattern, as discussed. Prolate spheroids of higher aspect ratios follow the sine-squared pattern even at $Re = 2000$. Oblate spheroids of aspect ratio 4 or larger do not exhibit the sine-squared pattern due to strong wake-induced drag. Regarding lift coefficients, we find that the theoretical C_L equation can provide a reasonable approximation, even at high Re, for prolate spheroids.

Both the drag law, valid at high Re for the prolate spheroids and low-aspect-ratio oblate spheroids, and the lift law for the prolate spheroids hold good potential for different applications. For example, they are very useful for Euler–Lagrangian flow simulations of non-spherical particles. Any particle-shape-specific C_D and C_L for a given Re at different ϕ, even at high Re, can be obtained by performing just two simulations: C_D at $\phi = 0^\circ$ and $\phi = 90^\circ$.

Acknowledgements

The authors thank the European Research Council for its financial support under its consolidator grant scheme, contract no. 615906 (NonSphereFlow). The simulations were performed in LB3D code with additional improvements. We thank Professor J. Harting for providing the code and Professor J. A. M. Kuipers for fruitful discussions. The first author thanks Dr A. Zarghami and Q. Xie for the interesting discussions on LBM. The work has been made possible by a grant for computation time, project number SH-351-15, financed by the Netherlands Organisation for Scientific Research (NWO).

References

AIDUN, C. K., LU, Y. & DING, E.-J. 1998 Direct analysis of particulate suspensions with inertia using the discrete Boltzmann equation. *J. Fluid Mech.* **373**, 287–311.

BOUZIDI, M., FIRDAOUSS, M. & LALLEMAND, P. 2001 Momentum transfer of a Boltzmann-lattice fluid with boundaries. *Phys. Fluids* **13**, 3452–3459.

EL KHOURY, G. K., ANDERSSON, H. I. & PETTERSEN, B. 2010 Crossflow past a prolate spheroid at Reynolds number of 10 000. *J. Fluid Mech.* **659**, 365–374.

EL KHOURY, G. K., ANDERSSON, H. I. & PETTERSEN, B. 2012 Wakes behind a prolate spheroid in crossflow. *J. Fluid Mech.* **701**, 98–136.

HAPPEL, J. & BRENNER, H. 1983 *Low Reynolds Number Hydrodynamics: with Special Applications to Particulate Media*. vol. 1. Springer.

HECHT, M. & HARTING, J. 2010 Implementation of on-site velocity boundary conditions for D3Q19 lattice Boltzmann simulations. *J. Stat. Mech. Theory Exp.* **2010**, P01018.

HÖLZER, A. & SOMMERFELD, M. 2009 Lattice Boltzmann simulations to determine drag, lift and torque acting on non-spherical particles. *Comput. Fluids* **38**, 572–589.

HUANG, H., YANG, X., KRAFCZYK, M. & LU, X.-Y. 2012 Rotation of spheroidal particles in Couette flows. *J. Fluid Mech.* **692**, 369–394.

https://doi.org/10.1017/jfm.2017.239 Published online by Cambridge University Press

D'HUMIÈRES, D., GINZBURG, I., KRAFCZYK, M., LALLEMAND, P. & LUO, L.-S. 2002 Multiple-relaxation-time lattice Boltzmann models in three dimensions. *Phil. Trans. R. Soc. Lond.* A **360**, 437–451.

JIANG, F., GALLARDO, J. P., ANDERSSON, H. I. & ZHANG, Z. 2015 The transitional wake behind an inclined prolate spheroid. *Phys. Fluids* **27**, 093602.

KRUGGEL-EMDEN, H., KRAVETS, B., SURYANARAYANA, M. K. & JASEVICIUS, R. 2016 Direct numerical simulation of coupled fluid flow and heat transfer for single particles and particle packings by a LBM-approach. *Powder Technol.* **294**, 236–251.

LALLEMAND, P. & LUO, L.-S. 2003 Lattice Boltzmann method for moving boundaries. *J. Comput. Phys.* **184**, 406–421.

OUCHENE, R., KHALIJ, M., ARCEN, B. & TANIÈRE, A. 2016 A new set of correlations of drag, lift and torque coefficients for non-spherical particles and large Reynolds numbers. *Powder Technol.* **303**, 33–43.

PAN, C., LUO, L.-S. & MILLER, C. T. 2006 An evaluation of lattice Boltzmann schemes for porous medium flow simulation. *Comput. Fluids* **35**, 898–909.

PLOUMHANS, P., WINCKELMANS, G. S., SALMON, J. K., LEONARD, A. & WARREN, M. S. 2002 Vortex methods for direct numerical simulation of three-dimensional bluff body flows: application to the sphere at $Re = 300$, 500, and 1000. *J. Comput. Phys.* **178**, 427–463.

VAKARELSKI, I. U., BERRY, J. D., CHAN, D. Y. C. & THORODDSEN, S. T. 2016 Leidenfrost vapor layers reduce drag without the crisis in high viscosity liquids. *Phys. Rev. Lett.* **117**, 114503.

ZASTAWNY, M., MALLOUPPAS, G., ZHAO, F. & VAN WACHEM, B. 2012 Derivation of drag and lift force and torque coefficients for non-spherical particles in flows. *Intl J. Multiphase Flow* **39**, 227–239.

https://doi.org/10.1017/jfm.2017.239 Published online by Cambridge University Press